Focusing through scattering media using integrated photonics

Filip Milojković,[*,†,‡] Niels Verellen,[*,†] Roelof Jansen,[†] Frédéric Peyskens,[†] Mathias Prost,[†] Jon Øyvind Kjellman,[†] Xavier Rottenberg,[†] and Pol Van Dorpe[†,‡]

†*imec, Kapeldreef 75, 3001 Leuven, Belgium*

‡*KU Leuven, Dept. of Physics and Astronomy, 3001 Leuven, Belgium*

E-mail: filip.milojkovic@imec.be; niels.verellen@imec.be

Abstract

A vast range of optical imaging techniques strives towards high-resolution imaging at elevated penetration depths. However, as the light travels through biological tissue it gets scattered, leading to image deterioration with increasing imaging depth. Consequentially, a number of wavefront shaping techniques have emerged - aiming to control the scattered light by tailoring the illumination wavefront. We propose a novel wavefront shaping device based on integrated photonics which, compared to the conventional liquid-crystal spatial light modulators, can improve on the modulation speed, pixel pitch, and reduce the overall optical path length of the system. These improvements are highly relevant for, e.g., in-vivo imaging of neural activity in a freely moving animal. The device relies on a one-dimensional optical phased array consisting of 128 emitters placed at 2.3 µm pitch and operates in the near-infrared spectral region ($\lambda = 1.55\,\mu m$). Using a photonic integrated circuit to modulate the wavefront phase, we demonstrate diffraction-limited focusing through static scatterers. Focus intensity

enhancements close to the maximum value predicted by the random matrix theory are experimentally achieved. Furthermore, our one-dimensional wavefront shaper can focus the scattered light over a two-dimensional grid, enabling raster scanning of the spot for imaging. Characterization of the phase modulators shows that the device is capable of modulation rates up to 5 kHz.

Keywords

Integrated photonics, wavefront shaping, scattering compensation microscopy, scattering media, optical phased array, silicon photonics

Introduction

Light scattering caused by refractive index inhomogeneity of biological tissue impedes conventional optical microscopy techniques from achieving high-resolution imaging at elevated depths. With the increase of imaging depth, the number of scattering events increases, exponentially reducing the number of ballistic, i.e. non-scattered, photons. Since conventional microscopy techniques rely on ballistic photons, their maximum imaging depth is fundamentally limited by the scattering. For example, this effect limits the imaging depth of widely used confocal microscopy to only a few hundreds of microns[1,2] in biological samples. On the other hand, the abundance of photons undergoing multiple scattering events deeper in the tissue[2,3] gives rise to the idea of controlling the scattered light in order to enable imaging at elevated depths. In 2007, Vellekoop and Mosk demonstrated that multiply scattered light can be refocused by iteratively optimizing the illumination wavefront,[4] founding the field of wavefront shaping in scattering media. Afterwards, it was shown that phase modulation of the wavefront is preferred over amplitude modulation because of the stronger focusing contrast.[5] Subsequent works[6–11] demonstrated that fast wavefront modulation is necessary for focusing in dynamic scattering samples. While offering phase modulation, commonly-

employed spatial light modulators (SLM) based on nematic liquid crystals on silicon (LCoS) offer only sub-kilohertz wavefront modulation rates.[12] This is insufficient for focusing in dynamic biological samples. An alternative are the SLMs based on micro electro-mechanics systems (MEMS). A Digital Micromirror Device (DMD) is a MEMS-based SLM, initially designed for display technologies, which offers fast operation with update rate typically higher than 20 kHz. However, they only provide amplitude modulation, making it a non-preferred choice for imaging in scattering media. We should note that phase modulation can be achieved using an amplitude-modulating SLM[13,14] in a holographic setup (Lee holography[15] e.g.). Nevertheless, that comes with a significant reduction in modulation power efficiency, meaning that only a few percent of power is actually modulated.[12] The preferred phase-modulating MEMS SLMs, based on deformable mirrors, offer fast wavefront modulation of around 10 kHz typically, but can be prohibitively expensive. Finally, Grating Light Valve (GLV) technology offers one-dimensional (1D) MEMS-based phase modulation at a remarkable update speed of 350 kHz enabling focusing in dynamic scattering media.[7] On the other hand, nonidealities present in the GLV modulator, such as gaps between the deformable mirrors and mirror curvature, noticeably reduce the quality of wavefront modulation, as explained in the supplement of Ref. 7.

Integrated photonics, as an alternative platform for wavefront shaping, offers competitive refresh rates and a significant reduction of the pixel pitch. In addition, a photonic integrated circuit (PIC) can provide both phase and amplitude modulation in a compact package compatible with large-scale fabrication. Recently, a transmitter-receiver pair of PICs has been employed for wavefront control in turbid media for improving the transmission through orthogonal channels in free space communication systems.[16] Here, we describe a PIC which can focus the light scattered by a static sample on a diffraction-limited spot and raster scan it over a two-dimensional grid, with the aim of enabling imaging within the scattering media. Our device is based on an optical phased array (OPA) which emits a phase-modulated wavefront as shown in Figure 1a. Differently from the majority of SLMs, which modulate

the laser beam in the reflection mode, light is first coupled to the photonic chip using a fiber and, after the modulation, outcoupled using optical antennas shown in Figure 1c. This presents a significant reduction in the overall optical path of the system, achieved by a compact PIC-based wavefront shaper. The need for compact wavefront shapers was highlighted in a recent publication,[17] as they could enable high-penetration in-vivo imaging of neural activity in freely moving animals. In such an application animals wear the imaging apparatus during the experiment. Therefore, the compactness of the wavefront shaper is of particular interest. The term optical antenna will be used interchangeably with optical emitter in this work.

The article is organized as follows: we first introduce the PIC and discuss the maximum phase modulation rate. Afterwards, the experimental methods are introduced. Then, the experiments on focusing through static scatterers are discussed. Finally, we show focusing over a two-dimensional grid, characterize the focused spot size and investigate the effect of the number of wavefront segments on the focus quality.

PIC Design

A PIC wavefront shaper is employed in our experiments as a replacement for commercially available SLMs. To modulate the wavefront of near-infrared light ($\lambda = 1.55\,\mu m$) we utilize a 1D array of 128 optical emitters with independently controlled phases, commonly referred to as the optical phased array (OPA). The device is fabricated on imec's hybrid 300mm photonics platform, which is detailed in the Ref. 18, featuring low-loss silicon nitride (SiN) and amorphous silicon (a-Si) waveguides. The cross-section of the stack is shown in Figure 1c. The platform offers the prospect of large-scale fabrication, as it's compatible with complementary metal-oxide-semiconductor (CMOS) technologies. As illustrated in Figure 1b, the PIC consists of the following functional blocks: power splitting section, phase modulation section, and optical emitter section. Laser light coming from an external source is coupled

into a low-loss SiN waveguide using an optical fiber. A multimode-interferometer (MMI) splitter tree subsequently distributes the power evenly over 128 waveguides. The phase of light in each waveguide is individually controlled using thermo-optic phase shifters. Figure 1c includes an illustration of such a phase shifter. To reduce the modulation power consumption, a-Si is chosen as the waveguiding material in the phase modulation section since it typically has five to ten times higher thermo-optic coefficient than SiN.[19,20] This allows for efficient phase modulation with measured efficiency of 8mW/π. Additionally, thermal isolation trenches were etched between the phase shifters in order to reduce the thermal crosstalk. Thermal isolation additionally improves phase modulation efficiency, which reduces power consumption on one hand, but on the other hand, it reduces the maximum modulation speed.[21] Finally, the light is emitted from the chip using full-etch SiN linear gratings with divergent emission centered at $\theta \sim 5^\circ$ with respect to the chip-surface normal. Simulation of antenna's normalized emission profile is shown in Figure 2. Antenna emission was simulated using Ansys Lumerical FDTD and its simulated radiation efficiency is 26%. We note that the antenna was not optimized for outcoupling efficiency in this proof-of-concept work. The antenna array pitch is 2.3µm, resulting in a compact OPA aperture size of $\sim 10 \times 300\mu m^2$. Table 1 shows comparison of our device to the commercially available (LCoS and MEMS-based) SLMs, reassuring that PIC can offer competitive performance in terms of pixel pitch and modulation speed. Compared to the smallest pixel pitch of commercially available phase-modulating SLMs, our device offers pixel pitch reduction - allowing for higher wavefront shaper pixel density.

Our OPA design can be scaled to higher antenna counts while conserving the pitch. Additionally, a recent LiDAR demonstration reassures that a 1D OPA can be scaled to $\sim 10^4$ antennas in a single reticle, and close to 5×10^4 if several reticles are combined in a super cell.[22] To put this into perspective, it was previously demonstrated that even 1020 SLM pixels is enough for scattering compensation in dynamic media with tissue-like scattering properties.[6] When increasing the element count, a potential issue is the high

power consumption associated with an increasing modulator count, which would call for the device's active cooling. Therefore, efforts should be directed at minimizing the power consumption of the phase modulation section. A good candidate for low-power-consumption modulators are the ones based on electro-optic effects, as detailed in the Modulation Speed subsection.

If the OPA was to be expanded to two dimensions (2D), the pixel pitch would scale with the array size.[23] This is because one needs to accommodate for more complex waveguide routing in the 2D case. Nevertheless, a scalable 2D OPA architecture with array-size-independent pixel pitch (9 µm), relying on bus waveguides and antennas with co-integrated phase modulators, has been previously demonstrated.[24]

Table 1: Comparison of the available phase-modulating SLMs and the PIC-based approach

Wavefront shaper	Modulation rate	Pixel pitch [µm]	Pixel count
LCoS SLM[12,25]	sub-kHz	3.74	$\sim 10^7$
1D OPA (this work)	5 kHz	2.3	128
Deformable mirrors[6,26]	5-10 kHz	10.8 - 400	$\sim 10^3$
1D GLV[7]	350 kHz	25.5	1088

Modulation Speed

The maximum operation frequency of the wavefront shaper is limited by the time constant of the thermal transient of the thermo-optic phase modulators. A change in waveguide temperature induced by running current through the resistive element in close proximity to the waveguide induces the optical phase shift. However, a direct measurement of the waveguide temperature is technically difficult. Therefore, we make use of a Mach-Zender interferometer (MZI) to extract the thermal time constant of the modulator. The MZI structure and its response are shown in Figure 3. In order to extract the thermal time constant of the modulator the small signal switching method was used. As illustrated in Figure 3a, the main idea of the method is to perform switching between the states which are in the approximately linear part of the MZI response ("small signal switching zone" in

Figure 3a). This way, the time constant of the observed optical transient corresponds to the thermal time constant. By fitting the transient data shown in Figure 3c, we obtain a thermal time constant $\tau = 33.5\,\mu s$. The phase modulator's maximum operating frequency therefore is $f_{max} = \frac{1}{2\pi\tau} \approx 5\,kHz$, which is significantly higher than a typical f_{max} of a LCoS SLM (sub-kHz).

Modulation rates of thermo-optic phase shifters can be increased using advanced driving schemes, at the cost of higher power consumption.[27] Additionally, alternative on-chip phase modulator architectures that are compatible with our device and operate in megahertz (MHz) or gigahertz (GHz) range, such as piezo-optomechanical[28] (100 MHz) or electro-optic (EO) modulators[29] ($> 10\,GHz$) are available for both near-infrared[30] and visible light.[31,32] Furthermore, a recent proof of concept demonstration shows that EO modulators can be used for PIC-based wavefront shaping with modulation rate up to 1.4 GHz on a lithium niobate platform.[33]

Moreover, EO modulators consume less power than the thermo-optic ones. Power consumption of the EO modulators, because of their capacitive nature, depends on the modulation frequency. At e.g. 5 kHz, their power consumption can be estimated to be at the nano-watt level from the reported energy-per-bit values.[34] This drastic reduction in power consumption compared to the thermo-optic modulators, makes EO modulation a favourable choice for large-scale OPAs. On the other hand, efforts should be devoted to reducing their size, as it is typically on a millimeter scale (lithium niobate-based modulators).

Experimental Methods

The experimental setup for focusing through scattering samples is presented in Figure 4. The PIC-based wavefront shaper is wire bonded on a PCB which establishes electrical connections between the on-chip phase modulators and the driver electronics (PIC driver in Figure 4). The in-coupling optical fiber and external laser source are shown in the same

figure. Light emitted from the chip is imaged on the scattering sample using a 20× objective with numerical aperture of NA = 0.4 and lens L1 with focal length f = 25mm. Scattered light speckle patterns are imaged onto a NIR camera (Goldeye G-130) using a 10× objective with NA = 0.26 and a lens (L2, f = 100mm).

We determine the optimal wavefront for focusing through the scattering sample using the continuous sequential iterative optimization method.[35] Before starting the optimization we choose the focusing target which is a single camera pixel. Since the field at the camera plane is a superposition of fields coming from all antennas in the OPA, we can find the optimal wavefront by optimizing the phase of each antenna individually. The phase of a single antenna is swept from 0 to 2π and the intensity at the target is recorded. Directly after the measurement, the antenna phase is set to the value which maximizes the target intensity. This process is repeated for all antennas in the array. Eight equidistant phase values over the 2π range are used for wavefront modulation. This number of phase values was chosen empirically as it presented the best trade-off between the execution time and the focused spot's peak-to-background ratio (PBR) in the experiment.

Previously, it was shown that a stripe-like elongated illumination on the scattering sample (coming from a 1D SLM) produces elongated speckle grains.[7] We observe the same effect for 1D OPA being imaged onto the scattering sample. In order to generate round speckle grains, shown in Figure 5a, we placed the scattering sample a few millimeters behind the focal plane of lens L1 ($\sim$ 4mm in our experiments). This way, due to the asymmetric divergence of the antenna emission (Figure 2), square-like sample illumination is achieved - resulting in round speckle grain formation.

Results and Discussion

Using the setup explained in the previous section, we demonstrate focusing through scattering samples using the PIC previously introduced. Two types of static scattering samples

were used: a ground glass diffuser with $\sim 15^\circ$ diffusion angle (Thorlabs DG10-120) and five layers of an opaque Parafilm M tape. These samples were chosen because of their good stability and forward scattering behaviour comparable to biological tissue. It was experimentally confirmed that Parafilm M has scattering properties similar to tissue in the supplement of Ref 36. Additionally, a ground glass diffuser is a common sample choice in the wavefront shaping community.[6,7,13,37,38]

Images of focusing through the ground glass diffuser are shown in Figure 5. In panel a, we see the initial speckle pattern generated when a non-optimized OPA wavefront impinges on the scattering sample. After the optimization, phase shifts which maximize the intensity in a single speckle grain, i.e. focused spot, are applied to the OPA. The resulting focused spot is shown in Figure 5b. However, even after the optimization there's certain light intensity outside the focused spot, i.e. background speckle. The background speckle might not be clearly visible in panel b because of camera's dynamic range. In order to overcome the limited camera's dynamic range we generated Hyper Dynamic Range (HDR) images using a method introduced by Debevec et al.[39] Five images of the focused spot taken at different integration times were used to reconstruct an HDR image, plotted in Figure 5c (logarithmic scale). Additionally, we show that generating a set of focused spots over a two dimensional grid is possible by forming a composite image of imec logo shown in Figure 5d. Focused spots forming the logo are generated one at a time and the final image is generated by summing the images of different spots. Scanning a focus over a 2D grid is also shown in the Supporting Video 2. A derivation showing that 2D focusing of scattered light is possible using 1D phase control is available in the supplementary information of Ref. 7. The evolution of the spot optimization is shown in the Supporting Video 1 (reproduction speed is 35 times the experimental speed). The final frame of the Supporting Video 1 is overexposed in order to show the background speckle.

The enhancement of the focused spot is defined as peak-to-background ratio (PBR) and calculated using the following formula: $\eta = I_p/\overline{I_b}$, where I_p is the peak intensity of the

focused spot, while $\overline{I_b}$ is the average background speckle intensity when the focus is formed. However, due to the limited dynamic range of the camera, background speckle and the focused spot could not be imaged simultaneously without under-exposing one or saturating the other part of the scene. Thus, once the optimized wavefront was applied and the focused spot was created, two images were acquired: one, so-called overexposed image, where the background speckle is inside the camera's dynamic range, but the focused spot is saturated; and the other one where the focused spot's intensity is inside camera's dynamic range. Average background speckle intensity was calculated by removing the saturated pixels from the overexposed image, as they belong to the focused spot, and then finding the average intensity in the rest of the image.

The evolution of the enhancement for the two scattering samples, i.e. ground glass diffuser and five layers of Parafilm M, is plotted in Figure 6a. The data is averaged over 25 experimental realizations per sample. Every experiment had $2N$ optimization steps, where $N = 128$ is the number of optical antennas on the PIC. After one full loop through the OPA antennas, i.e. after 128 iterations, the enhancement value stabilizes as shown in Figure 6a. Enhancement values achieved are $\eta = 90 \pm 6$ in case of the ground glass diffuser, and $\eta = 70 \pm 9$ in case of five Parafilm M layers. The enhancement when focusing through the ground glass diffuser is close to the maximum value predicted by the random matrix theory[5] $\eta = \pi/4 * (N - 1) + 1 \approx 100$. Previously, it was demonstrated that a GLV 1D SLM with 128 segments can achieve enhancements around 30 when focusing through a ground glass diffuser.[7] As shown in the supplementary information of Ref. 7, the reflection from GLV's back surface, i.e. non-modulated patches of the wavefront, impede the experimental enhancement from reaching the theoretical maximum. Our device does not suffer from such issue and modulates the full emitted wavefront enabling experimental enhancements very close to the theoretical maximum.

The lower enhancement values observed when focusing through Parafilm M are caused by the shorter speckle persistence times observed for this sample. For a given sample, speckle

persistence time is the time scale over which the speckle pattern remains stable. Shorter speckle persistence times are potentially caused by a variation in the size of the gaps between the Parafilm layers throughout the experiment. It was previously shown that a decrease in speckle persistence time results in a decrease of experimentally achievable enhancements.[4]

Enhancement versus the number of wavefront segments

Random matrix theory predicts that the enhancement η linearly depends on the number of wavefront segments N_s used to perform wavefront phase control. The theoretic dependence is given by the formula:[5] $\eta = \pi/4 * (N_s - 1) + 1$. In our experimental study, a wavefront segment was defined as a group of adjacent antennas with a common phase shift applied. As shown in Figure 6b, the experimental data follows the theoretical model. The enhancement values for $N_s <= 32$ are higher than the model's prediction possibly due to the fact that the optimization target (single camera pixel) was at a local speckle intensity maximum. This particular local intensity maximum, i.e. speckle grain, had a high PBR ratio of approx. 10 before the optimization. In other words, there was a PBR bias at the target prior to the optimization. This PBR bias leads to increased η values for lower N_s, since the enhancement itself is defined as the PBR ratio. Such a target was chosen to secure the optimization convergence, as the algorithm needs certain signal-to-noise ratio to be able to converge.

Focused spot size

We investigate the size of the generated focus spot using a similar approach as the one presented in the Ref. 40. To this end, we vary the distance behind the sample at which the focused spot is generated and record the full width at half maximum (FWHM) of the generated spot. This data is shown in Figure 7a. In case of diffraction on a circular aperture, an Airy pattern is generated in the far field. Therefore, the FWHM of a diffraction-limited spot created by a perfect lens with circular aperture is given by the Airy pattern: FWHM $= \frac{1.03\lambda}{D} f$, where λ is the wavelength, D is the aperture diameter and f is the focusing distance. If

we assume that the spot in our experiments is diffraction limited, using the above formula together with the polynomial coefficient of the fit in Figure 7a, we can calculate the corresponding aperture size D. In our case, D represents the diameter of the illumination projected by the OPA on the scattering sample. A simple calculation gives that this sample illumination diameter is 1 mm. When comparing to the actual experimental illumination profile shown in Figure 7b it is observed that the horizontal extent of the illumination is on the order of one millimeter (see scale bar for reference). This indicates that the generated focused spot size is diffraction limited. Differently from the experiment presented in Figure 5, where symmetric sample illumination resulted in a round focused spot, we note that the horizontal and vertical illumination extents are not equal in this experiment (Figure 7b). This results in different diffraction limited spot sizes for the two directions (elliptical spot). Repeating the calculation for the vertical direction, results in $D = 165\,\mu m$. Also this value matches the vertical extent of the illumination's main lobe (Figure 7b). For clarity and simplicity, the graph in panel a shows only the data and the fit for the horizontal direction. Finally, even though the formula for diffraction limited FWHM is derived for the case of a plane wave in normal incidence on a circular aperture, we find good agreement with the spot's FWHM in our experiments where a more complex diffuser illumination wavefront is present. This is also in agreement with the results shown in the Ref. 40.

Conclusion

We demonstrated integrated photonics-based focusing through static scattering media using a one-dimensional optical phased array with 128 antennas. The device, with an operational wavelength of 1550 nm, has an emitter array pitch of 2.3 µm. Intensity enhancement factors close to the theoretical maximum were demonstrated. Furthermore, it was shown that our PIC-based wavefront shaper enables diffraction-limited focusing over a two-dimensional grid, while using only a one-dimensional wavefront shaper. The device was fabricated in the imec

300mm CMOS pilot line using a hybrid a-Si/SiN platform which offers the prospect of large-scale fabrication. The PIC employs thermo-optic phase shifters with measured thermal time constant of 33.5 µs, allowing for modulation rates up to approximately 5 kHz. Compared to the conventional liquid-crystal SLMs, our device offers an increase in the modulation rate and pixel pitch reduction. The latter leads to a reduction in the device footprint, which is highly relevant for, e.g., in-vivo experiments where a freely moving animal wears the imaging apparatus.[41–43] Additionally, a recent study emphasizes the need for a compact wavefront shaper to enable imaging of neural activity at depth in freely moving animals.[17] Thus, PIC improvements in device compactness compared to reflective-mode SLMs, which are detailed in the Introduction, are advantageous for this application. In addition, as detailed in the Modulation Speed subsection, replacing a thermo-optic modulator with one of the compatible electro-optic modulators would enable on-chip wavefront shaping at GHz rates and reduce the modulator power consumption. Integration of a laser on the same photonic chip, by means of flip-chip bonding[44] or micro-transfer printing,[45] could enable a very compact PIC wavefront shaper. Shifting the working wavelength towards the visible will enable fluorescent imaging in turbid media. We believe that these results will lead to innovative approaches in deep tissue imaging with integrated photonics as an exciting platform for wavefront shaping.

Supporting Information Available

Videos of: spot optimization (Supporting_Video_1.avi) and scanning of pre-calibrated spots over a 2D grid (Supporting_Video_2.avi). Supporting_Video_1.avi reproduction speed is 35 times the actual experimental speed and the final frame of the video is over-exposed in order to show the background speckle. This material is available free of charge via the Internet at http://pubs.acs.org

References

(1) Ntziachristos, V. Going deeper than microscopy: the optical imaging frontier in biology. *Nature Methods* **2010**, *7*, 603–614.

(2) Yoon, S.; Kim, M.; Jang, M.; Choi, Y.; Choi, W.; Kang, S.; Choi, W. Deep optical imaging within complex scattering media. *Nature Reviews Physics* **2020**, *2*, 141–158.

(3) Kang, S.; Jeong, S.; Choi, W.; Ko, H.; Yang, T. D.; Joo, J. H.; Lee, J.-S.; Lim, Y.-S.; Park, Q.-H.; Choi, W. Imaging deep within a scattering medium using collective accumulation of single-scattered waves. *Nature Photonics* **2015**, *9*, 253–258.

(4) Vellekoop, I. M.; Mosk, A. P. Focusing coherent light through opaque strongly scattering media. *Optics Letters* **2007**, *32*, 2309.

(5) Vellekoop, I. M. Feedback-based wavefront shaping. *Optics Express* **2015**, *23*, 12189.

(6) Blochet, B.; Bourdieu, L.; Gigan, S. Focusing light through dynamical samples using fast continuous wavefront optimization. *Optics Letters* **2017**, *42*, 4994.

(7) Tzang, O.; Niv, E.; Singh, S.; Labouesse, S.; Myatt, G.; Piestun, R. Wavefront shaping in complex media with a 350 kHz modulator via a 1D-to-2D transform. *Nature Photonics* **2019**, *13*, 788–793.

(8) Blochet, B.; Joaquina, K.; Blum, L.; Bourdieu, L.; Gigan, S. Enhanced stability of the focus obtained by wavefront optimization in dynamical scattering media. *Optica* **2019**, *6*, 1554.

(9) Blochet, B.; Akemann, W.; Gigan, S.; Bourdieu, L. Fast wavefront shaping for two-photon brain imaging with large field of view correction. 2021, 2021.09.06.459064; *bioRxiv*. `https://doi.org/10.1101/2021.09.06.459064` (accessed September 19, 2024).

(10) Gigan, S. et al. Roadmap on wavefront shaping and deep imaging in complex media. *Journal of Physics: Photonics* **2022**, *4*, 042501.

(11) Hsieh, C.-M.; Malik, M. O. A.; Liu, Q. High-speed feedback based wavefront shaping for spatiotemporal enhancement of incoherent light through dynamic scattering media. *Optics Letters* **2023**, *48*, 2313.

(12) Cao, H.; Čižmár, T.; Turtaev, S.; Tyc, T.; Rotter, S. Controlling light propagation in multimode fibers for imaging, spectroscopy, and beyond. *Advances in Optics and Photonics* **2023**, *15*, 524.

(13) Conkey, D. B.; Caravaca-Aguirre, A. M.; Piestun, R. High-speed scattering medium characterization with application to focusing light through turbid media. *Optics Express* **2012**, *20*, 1733.

(14) Gomes, A. D.; Turtaev, S.; Du, Y.; Čižmár, T. Near perfect focusing through multimode fibres. *Optics Express* **2022**, *30*, 10645.

(15) Lee, W.-H. III Computer-Generated Holograms: Techniques and Applications. In *Progress in Optics*. Elsevier **1978**, *16*, 119–232.

(16) SeyedinNavadeh, S.; Milanizadeh, M.; Zanetto, F.; Ferrari, G.; Sampietro, M.; Sorel, M.; Miller, D. A. B.; Melloni, A.; Morichetti, F. Determining the optimal communication channels of arbitrary optical systems using integrated photonic processors. *Nature Photonics* **2023**, *18*, 149–155.

(17) Xia, F.; Rimoli, C. V.; Akemann, W.; Ventalon, C.; Bourdieu, L.; Gigan, S.; de Aguiar, H. B. Neurophotonics beyond the surface: unmasking the brain's complexity exploiting optical scattering. *Neurophotonics* **2024**, *11*, S11510.

(18) Marinins, A.; Kjellman, J.; Prost, M.; Kongnyuy, T. D.; Saseendran, S.; Dahlem, M. S.; Rottenberg, X.; Jansen, R.; Soussan, P. Bragg Reflector Co-integrated with SiN and

a-Si on 300 mm Wafers for Low Loss Optical Beamformers. Conference on Lasers and Electro-Optics. San Jose, California, 2022; p SM4G.6.

(19) Komma, J.; Schwarz, C.; Hofmann, G.; Heinert, D.; Nawrodt, R. Thermo-optic coefficient of silicon at 1550 nm and cryogenic temperatures. *Applied Physics Letters* **2012**, *101*, 041905.

(20) Arbabi, A.; Goddard, L. L. Measurements of the refractive indices and thermo-optic coefficients of Si_3N_4 and SiO_x using microring resonances. *Optics Letters* **2013**, *38*, 3878.

(21) Masood, A.; Pantouvaki, M.; Lepage, G.; Verheyen, P.; Van Campenhout, J.; Absil, P.; Van Thourhout, D.; Bogaerts, W. Comparison of heater architectures for thermal control of silicon photonic circuits. 10th International Conference on Group IV Photonics. Seoul, Korea (South), 2013; pp 83–84.

(22) Guglielmon, J.; Byrd, M. J.; Moss, B. R.; Tran, J.; Millman, R. P.; Watts, M. R.; Poulton, C. V. Optical Phased Array Super-Cell Beyond the Reticle Limit. CLEO 2023. San Jose, CA, 2023; p STh5C.5.

(23) Fatemi, R.; Khachaturian, A.; Hajimiri, A. A Nonuniform Sparse 2-D Large-FOV Optical Phased Array With a Low-Power PWM Drive. *IEEE Journal of Solid-State Circuits* **2019**, *54*, 1200–1215.

(24) Sun, J.; Timurdogan, E.; Yaacobi, A.; Hosseini, E. S.; Watts, M. R. Large-scale nanophotonic phased array. *Nature* **2013**, *493*, 195–199.

(25) GAEA-2 10 Megapixel Phase Only LCOS-SLM - HOLOEYE Photonics AG. 2023; `https://holoeye.com/products/spatial-light-modulators/gaea-2-phase-only/`.

(26) Byrum, T. M.; Oberascher, K.; Walker, Z.; Lyubarsky, A.; Martin, S.; Orr, G.; McDonald, W.; Gilly, N.; O'Brien, S.; Taylor, K.; Hamlin, W.; Oden, P.; Hall, J. Optimizing a micro electro mechanical system (MEMS) based phase-only light modulator (PLM) for improved system performance. Emerging Digital Micromirror Device Based Systems and Applications XVI. San Francisco, United States, 2024; pp 88–95.

(27) Della Corte, F. G. Modulation speed improvement in a Fabry–Perot thermo-optical modulator through a driving signal optimization technique. *Optical Engineering* **2009**, *48*, 074601.

(28) Dong, M.; Clark, G.; Leenheer, A. J.; Zimmermann, M.; Dominguez, D.; Menssen, A. J.; Heim, D.; Gilbert, G.; Englund, D.; Eichenfield, M. High-speed programmable photonic circuits in a cryogenically compatible, visible–near-infrared 200 mm CMOS architecture. *Nature Photonics* **2022**, *16*, 59–65.

(29) Zhang, M.; Wang, C.; Kharel, P.; Zhu, D.; Lončar, M. Integrated lithium niobate electro-optic modulators: when performance meets scalability. *Optica* **2021**, *8*, 652.

(30) Celik, O. T.; Sarabalis, C. J.; Mayor, F. M.; Stokowski, H. S.; Herrmann, J. F.; McKenna, T. P.; Lee, N. R. A.; Jiang, W.; Multani, K. K. S.; Safavi-Naeini, A. H. High-bandwidth CMOS-voltage-level electro-optic modulation of 780 nm light in thin-film lithium niobate. *Optics Express* **2022**, *30*, 23177–23186.

(31) Desiatov, B.; Shams-Ansari, A.; Zhang, M.; Wang, C.; Lončar, M. Ultra-low-loss integrated visible photonics using thin-film lithium niobate. *Optica* **2019**, *6*, 380.

(32) Li, C.; Chen, B.; Ruan, Z.; Wu, H.; Zhou, Y.; Liu, J.; Chen, P.; Chen, K.; Guo, C.; Liu, L. High modulation efficiency and large bandwidth thin-film lithium niobate modulator for visible light. *Optics Express* **2022**, *30*, 36394.

(33) Zhong, H.; Zheng, Y.; Sun, J.; Wang, Z.; Wu, R.; Zhang, L.-e.; Liang, Y.; Hua, Q.; Ning, M.; Ji, J.; Fang, B.; Li, L.; Li, T.; Cheng, Y.; Zhu, S. Gigahertz-rate-switchable

wavefront shaping through integration of metasurfaces with photonic integrated circuit. *Advanced Photonics* **2024**, *6*, 016005.

(34) Rahim, A.; Hermans, A.; Wohlfeil, B.; Petousi, D.; Kuyken, B.; Van Thourhout, D.; Baets, R. Taking silicon photonics modulators to a higher performance level: state-of-the-art and a review of new technologies. *Advanced Photonics* **2021**, *3*, 024003–024003.

(35) Vellekoop, I.; Mosk, A. Phase control algorithms for focusing light through turbid media. *Optics Communications* **2008**, *281*, 3071–3080.

(36) Boniface, A.; Blochet, B.; Dong, J.; Gigan, S. Noninvasive light focusing in scattering media using speckle variance optimization. *Optica* **2019**, *6*, 1381.

(37) Yang, J.; He, Q.; Liu, L.; Qu, Y.; Shao, R.; Song, B.; Zhao, Y. Anti-scattering light focusing by fast wavefront shaping based on multi-pixel encoded digital-micromirror device. *Light: Science & Applications* **2021**, *10*, 149.

(38) Mastiani, B.; Osnabrugge, G.; Vellekoop, I. M. Wavefront shaping for forward scattering. *Optics Express* **2022**, *30*, 37436.

(39) Debevec, P. E.; Malik, J. Recovering high dynamic range radiance maps from photographs. ACM SIGGRAPH 2008 Classes. New York, NY, USA, 2008.

(40) Vellekoop, I. M.; Lagendijk, A.; Mosk, A. P. Exploiting disorder for perfect focusing. *Nature Photonics* **2010**, *4*, 320–322.

(41) de Groot, A.; van den Boom, B. J.; van Genderen, R. M.; Coppens, J.; van Veldhuijzen, J.; Bos, J.; Hoedemaker, H.; Negrello, M.; Willuhn, I.; De Zeeuw, C. I.; Hoogland, T. M. NINscope, a versatile miniscope for multi-region circuit investigations. *eLife* **2020**, *9*, e49987.

(42) Guo, C.; Blair, G. J.; Sehgal, M.; Jimka, F. N. S.; Bellafard, A.; Silva, A. J.; Golshani, P.; Basso, M. A.; Blair, H. T.; Aharoni, D. Miniscope-LFOV: A large-field-of-

view, single-cell-resolution, miniature microscope for wired and wire-free imaging of neural dynamics in freely behaving animals. *Science Advances* **2023**, *9*, eadg3918.

(43) Barbera, G.; Liang, B.; Zhang, L.; Li, Y.; Lin, D.-T. A wireless miniScope for deep brain imaging in freely moving mice. *Journal of Neuroscience Methods* **2019**, *323*, 56–60.

(44) Tanaka, S.; Jeong, S.-H.; Sekiguchi, S.; Kurahashi, T.; Tanaka, Y.; Morito, K. High-output-power, single-wavelength silicon hybrid laser using precise flip-chip bonding technology. *Optics Express* **2012**, *20*, 28057.

(45) Roelkens, G. et al. Present and future of micro-transfer printing for heterogeneous photonic integrated circuits. *APL Photonics* **2024**, *9*, 010901.

TOC Graphic

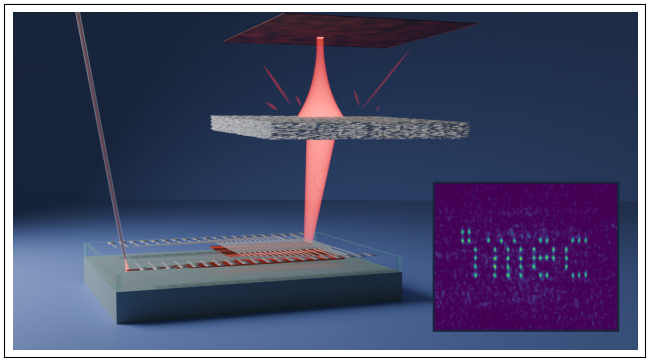

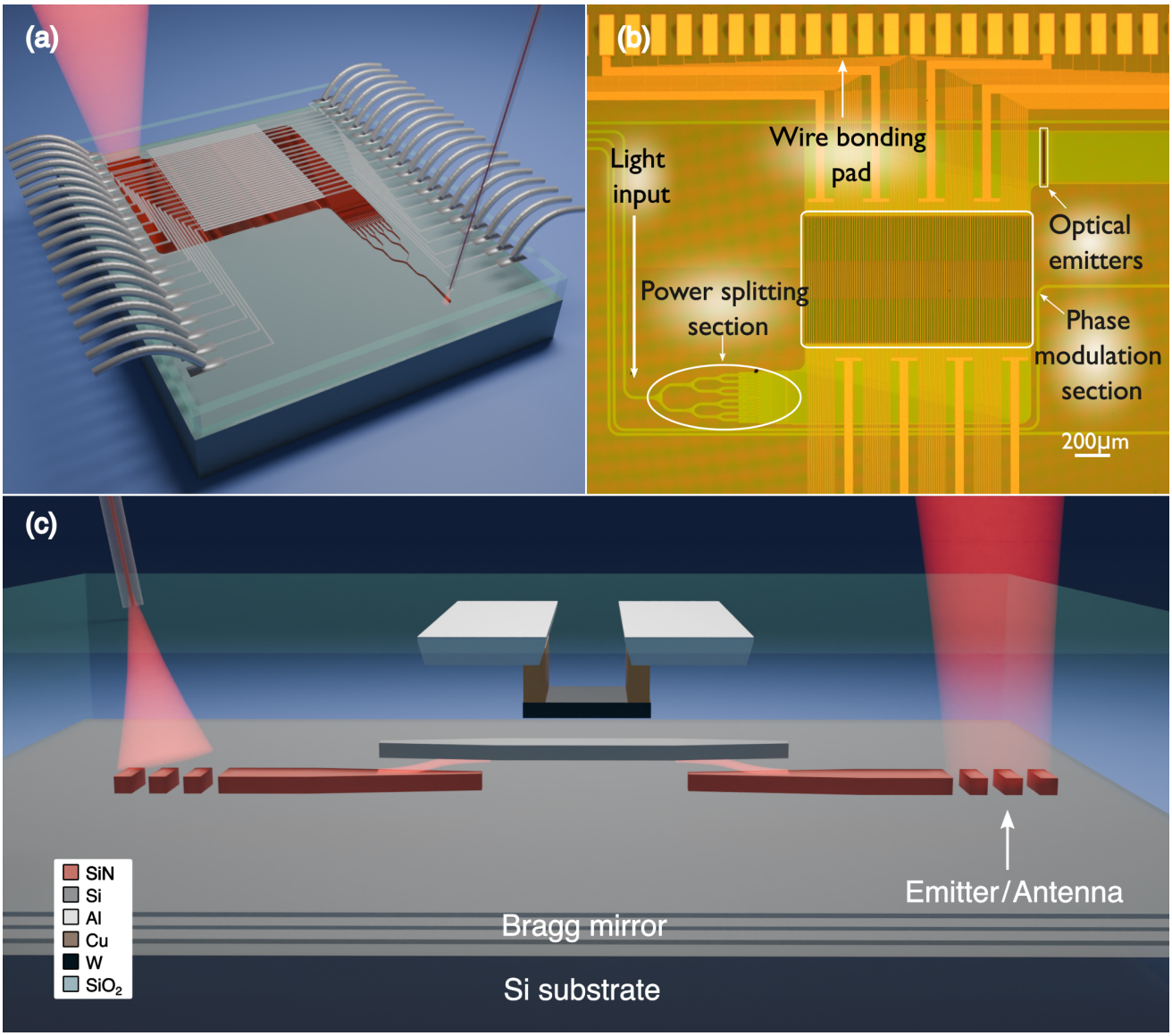

Figure 1: Photonic chip employed as a wavefront shaper. (a) Illustration of the chip. Laser emission coming from an external source is coupled into the chip using an optical fiber and after phase modulation outcoupled through optical emitters (linear gratings). (b) Microscope image of the chip with functional blocks marked. (c) Chip cross section illustration. SiN waveguide is used for light incoupling, routing and emission from the chip. Phase modulation happens in a-Si waveguide, by running current through a tungsten heating element in the waveguide's proximity. Light transfer between SiN and a-Si waveguides relies on the evanescent coupling. Bragg mirror is used to improve the efficiency of the incoupling grating and the OPA antennas.

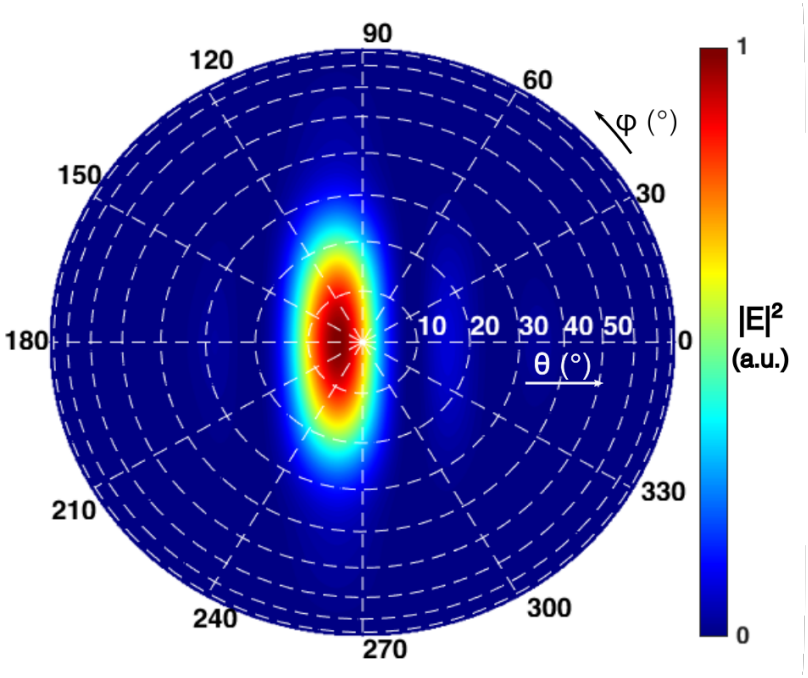

Figure 2: Simulation of the antenna's far field radiation pattern, i.e. normalized intensity of a single optical antenna (arbitrary units - a.u.). The horizontal axis on the graph corresponds to the antenna grating direction. Emission intensity is normalized to its maximum value.

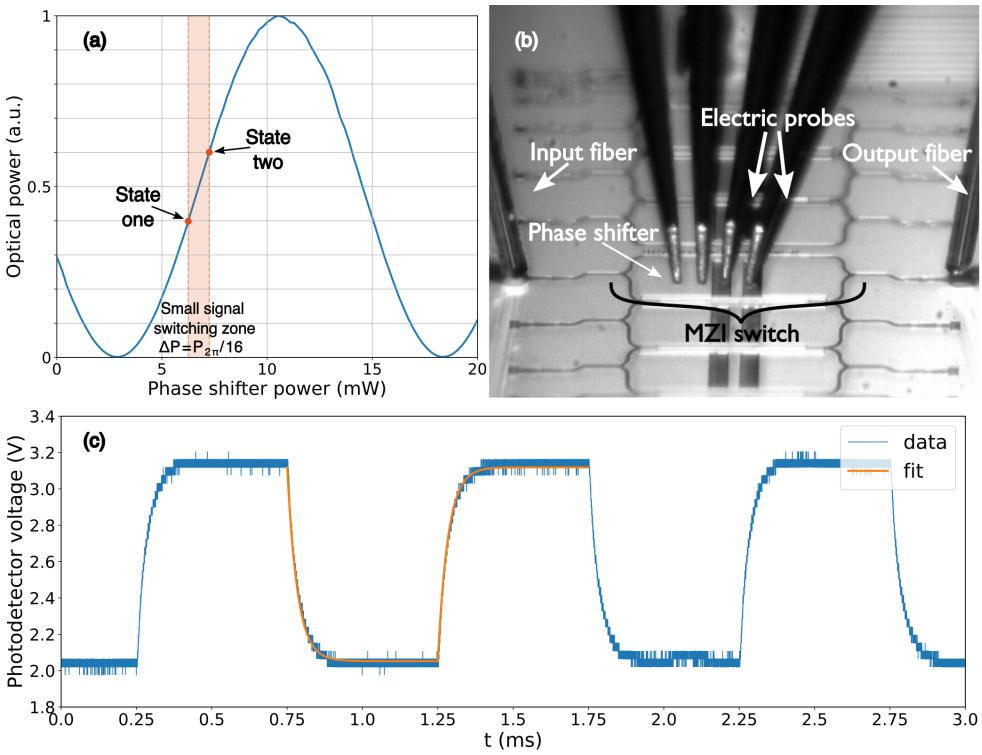

Figure 3: Measurement of the phase shifter transient response. (a) Small signal switching experiment for extracting the thermal time constant of the phase modulator. Applied power difference between the two states equals $\Delta P = P_{2\pi}/16 = 1\text{mW}$, resulting in $\pi/8$ phase shift. $P_{2\pi}$ is the modulator power needed for the 2π phase shift. (b) Experimental setup for measuring the transient response of a Mach-Zender interferometer (MZI) with thermo-optic phase shifter. (c) Transient response of MZI when driving phase shifter with 1 kHz square-wave pulses. The fitted thermal time constant is $\tau = 33.5\,\mu\text{s}$.

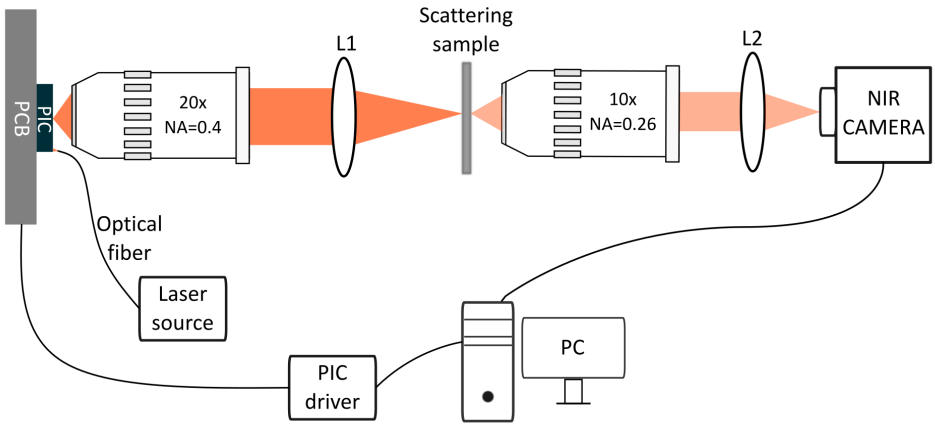

Figure 4: Illustration of the experimental setup. Light emitted from the photonic integrated circuit (PIC) is imaged on the scattering sample by means of a 20× objective and lens L1 ($f = 25\,\mathrm{mm}$). A 10 × objective and a lens (L2, $f = 100\,\mathrm{mm}$) image the speckle pattern (from a plane behind the sample) onto the NIR camera. The readout value of a single camera pixel is used as the feedback signal for the PIC phase-optimization algorithm running on a PC. The PIC chip is wire bonded to a printed circuit board (PCB) which provides the electrical connection to the PIC driving electronics.

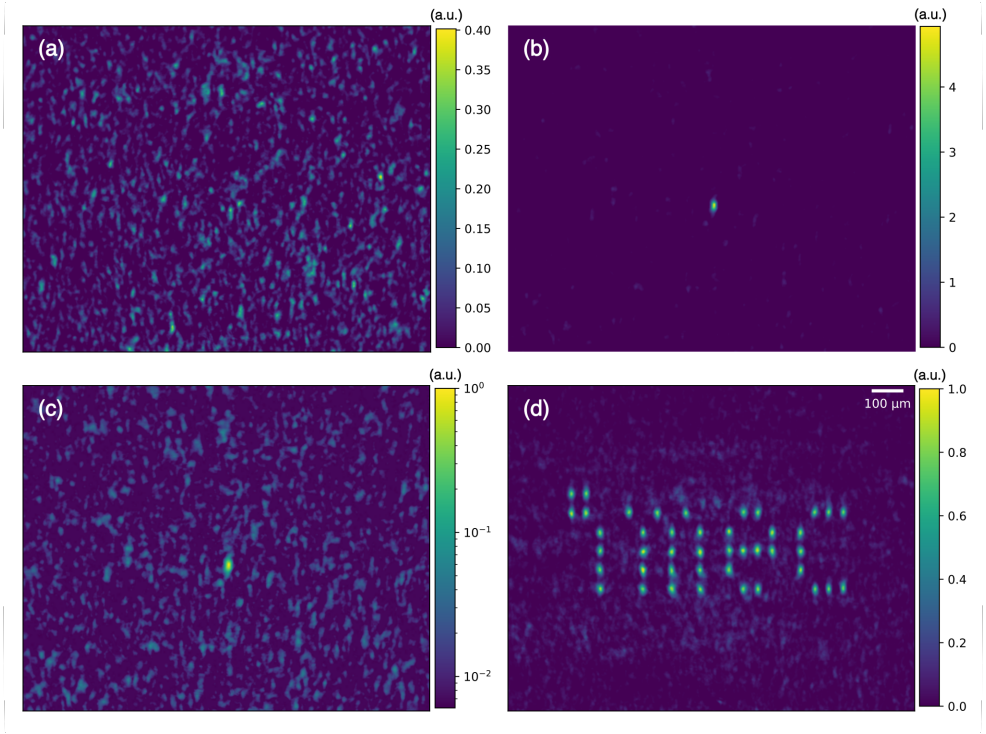

Figure 5: Images of focusing through a ground glass diffuser using a PIC-based wavefront shaper. Speckle pattern image before (a) and after (b) the optimization. Enhancement after the optimization is 91. Images (a) and (b) are scaled with respect to camera integration time and plotted in arbitrary units (a.u.). (c) Hyper Dynamic Range (HDR) version of the image in panel b (logarithmic scale normalized to the peak intensity) (d) Imec logo formed by the focused spots at different locations in the field of view. Focused spots in (d) are generated one at a time and the final image is generated by summing the images of different focused spots.

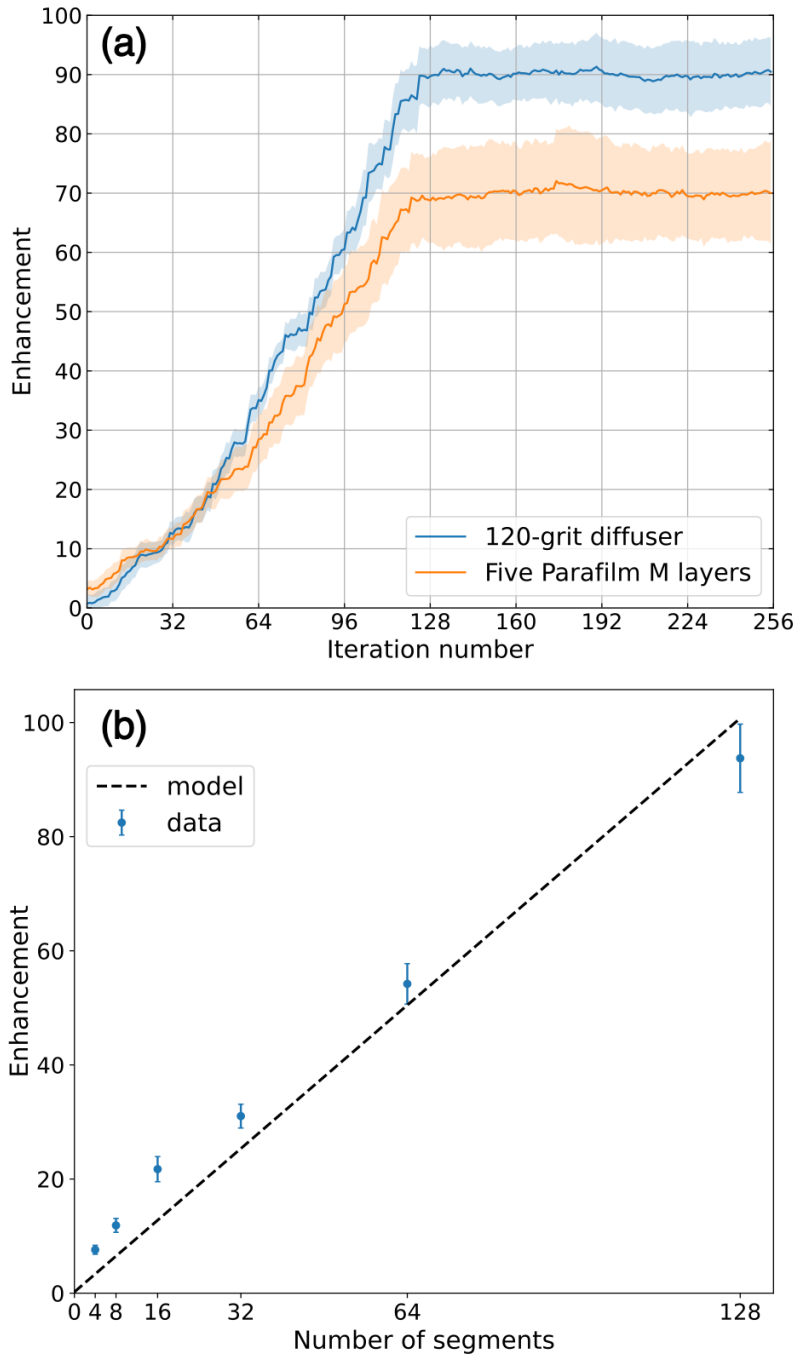

Figure 6: Enhancement characterization. (a) Evolution of the enhancement factor throughout the optimization. Experiments were performed on two samples: ground glass diffuser and five layers of Parafilm M. $2N$ optimization iterations were performed, where $N = 128$ is the number of optical antennas on the chip. 25 experiments were performed for every sample and the average enhancement (dark line) is plotted together with the standard deviation (light bands). (b) Enhancement as a function of the number of wavefront segments used. A wavefront segment is a group of adjacent antennas with a common phase shift. Data points show the mean value and standard deviation over 10 experiments using a ground glass diffuser as the scattering sample.

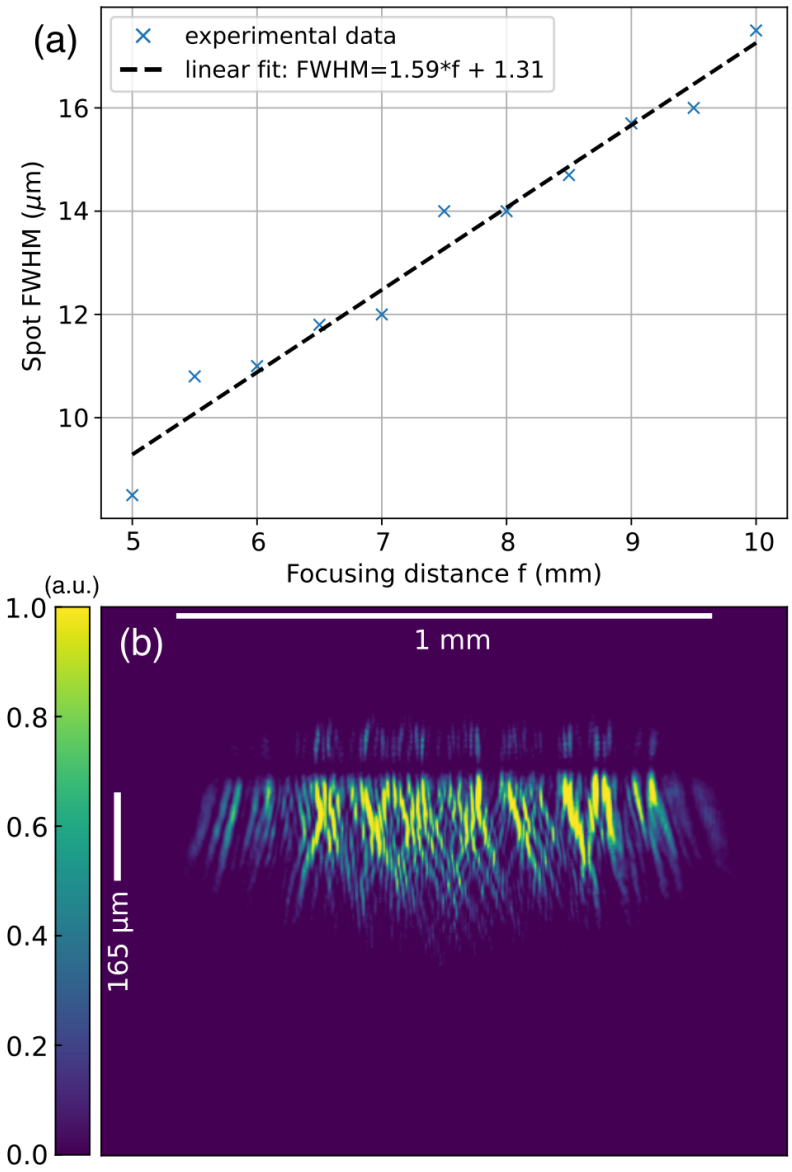

Figure 7: Diffraction-limited focusing. (a) Spot full width at half maximum (FWHM) as a function of the focusing distance f (distance behind the diffuser at which the focus is formed). (b) Illumination of the scattering sample. Focus FWHM over the horizontal axis is plotted in panel a. Scattering sample is a ground glass diffuser.